# Electronic Supplementary Information

## Z-Scheme heterojunction formation between $CsPbBr_3$ and BiOBr: Key to singlet oxygen formation for selective semidehydrogenation of tetrahydroisoquinoline

*Vishesh Kumar, Sunil Kumar Patel, Shivali Dhingra, Deepak Kumar, Ved Vyas, Kamalakannan Kailasam,* E. Siva Subramaniam Iyer,* and Arindam Indra**

V. Kumar, D. Kumar, Dr. V. Vyas, Prof. A. Indra
Department of Chemistry, Indian Institute of Technology (BHU), Varanasi, UP-221005, India.
E-mail: arindam.chy@iitbhu.ac.in

S. K. Patel, Prof. E. S. Subramaniam Iyer
School of Chemical and Materials Sciences, Indian Institute of Technology Goa, Ponda, Goa, India.
Email: essiyer@iitgoa.ac.in

S. Dhingra, Prof. Kamalakannan Kailasam
Advanced Functional Nanomaterials, Institute of Nano Science and Technology (INST), Knowledge City, Sector-81, Manauli, SAS Nagar, 140306 Mohali, Punjab, India.
E-mail: kamal@inst.ac.in

**Chemicals**

All chemicals are of analytical grade and used without further purification.

Lead(II) bromide (99.9%), cesium bromide, oleic acid (OA, 90%), oleylamine (OAm, 90%), dimethyl sulfoxide (DMSO), titanium butoxide, Sodium tungstate dihydrate, propane-2-ol, and 1-octadecene (ODE, 91%) were purchased from Sigma-Aldrich. Tetrabutylammonium hexafluorophosphate ($TBHPF_6$) and 9,10-diphenylanthracene (DPA) were purchased from BLD Pharma. Bismuth(III) nitrate pentahydrate, potassium bromide, ethyl acetate ($CH_3COOC_2H_5$, 99.9%), hexane (99.9%), tetrahydrofuran (THF), acetonitrile, toluene, isopropanol (IPA), methanol, and ethanol were purchased from Merck. Cadmium nitrate hexahydrate and ethylenediamine were purchased from SRL. *P*-Nitro-Blue tetrazolium chloride (NBT), *o*-tolidine, and 1,2,3,4-Tetrahydroisoquinoline (THIQ) were purchased from Sigma-Aldrich. Chloroform-d ($CDCl_3$), thiourea, and silica gel were purchased from Merck. All substrates were purchased from either Sigma-Aldrich, SRL, Merck, or Avra Chemicals.

**Instruments**

The crystal structure of the catalysts was confirmed using High-Resolution X-ray Diffraction (HR-XRD) on a Rigaku Smart Lab 9 kW Powder X-ray diffractometer (RIGAKU Corporation). Energy dispersive X-ray (EDX) spectroscopy studies were performed in a Team Pegasus Integrated EDS-EBSD system with Octane Plus and Hikari Pro. Elemental mapping was performed with an analyzer attached to the SEM. Transmission electron microscopy (TEM) studies were carried out on a Tecnai G2 20 TWIN transmission electron microscope, equipped with an energy-dispersive X-ray spectrometer (EDAX, r-TEM SUTW). For TEM mapping analysis, the JEOL JEM-2100 instrument was used and operated at 120 kV accelerating voltage.

X-ray photoelectron spectroscopy (XPS) measurements were conducted using a K-Alpha X-ray photoelectron spectrometer from Thermo Fisher Scientific. The binding energies were calibrated with the C 1s peak at 284.6 eV as the reference.

The UV-diffuse reflectance spectroscopy (DRS) measurements were performed using UV-vis spectroscopy with a Shimadzu UV-2600 spectrophotometer.

The detection of reactive oxygen species (ROS) and $H_2O_2$ was performed using the UV-Vis spectra of the complexes, recorded with an Agilent Cary 60 UV-Vis spectrophotometer.

$^1$H-NMR spectra were recorded using an AVH D 500 AVANCE III HD 500 MHz NMR spectrometer from Bruker BioSpin International. Chemical shifts are reported in ppm, and coupling constants are expressed in Hertz (Hz). The following abbreviations are used: s =

singlet, bs = broad singlet, d = doublet, t = triplet, and m = multiplet. Residual solvent signals were used as references for $^{1}H$ and $^{13}C$ NMR spectra ($CDCl_3$: $\delta_H$ = 7.28-7.29 ppm, $\delta_C$ = 77.01-77.16 ppm).

Electron paramagnetic resonance (EPR) studies were performed at room temperature using Bruker A300-9.5/12/S/W. The authors thank the Central Research Facility, IIT Delhi (Sonepat campus) for the EPR measurements.

Kelvin probe force microscopy (KPFM) measurements were carried out using an Asylum Research MFP-3D Origin + atomic force microscope under ambient conditions. An ElectriMulti75-G force modulation AFM probe (Budget Sensors) with a platinum-coated conductive cantilever (spring constant: ~3 N/m, resonance frequency: ~75 kHz) was used for the KPFM experiments.

HR-MS (m/z) were recorded on a SCIEX X500R QTOF in electron ionization or electrospray ionization (ESI) mode.

Light source: (JACKAL, LED 3-Watt blue light, 460 nm). 5 Lights were used together.

**Ultrafast transient absorption**

The ultrafast transient absorption (TA) experimental arrangement utilized an 80 MHz mode-locked laser. The samples were kept in a sealed quartz cuvette with a path length of 2 mm. The samples used in the experiments were suspended in Toluene and the OD was maintained ~0.3 in 2 mm path length. The sample was stirred using a magnetic stirrer. The pump wavelength of 370 nm (10 nJ) was generated from Operasolo OPA. A White light probe was created by focusing a segment of the amplified output center at 800 nm generated by an Astrella amplifier from Coherent USA operating at 1kHz, on a $CaF_2$ Crystal. The white light was split using a beam splitter to generate both signal and reference beams. These beams were directed through a fiber coupling unit to the detector (photodiode detector array) to capture the pump-induced changes at various delay times of the probe beam. All spectra were chirp corrected and measurement was conducted delay time window of up to 6 ns. The TA spectra are analyzed using Surface Explorer, V.4.2 software.

**Experimental**

**Synthesis of $CsPbBr_3$**

Initially, a Cs-OA precursor stock solution was prepared by adding $Cs_2CO_3$ (130 mg), ODE (10 mL), and OA (1 mL) in a 50 mL three-neck flask, heated at 120 °C for 1 hour under the $N_2$ atmosphere, then heated to 150 °C in $N_2$ until all $Cs_2CO_3$ reacted with OA, which was stored

at room temperature and preheated to 140 °C before use. Subsequently, $PbBr_2$ (72 mg), ODE (20 mL), OAm (1.0 mL), and OA (1.0 mL) were introduced into a 25 mL three-neck flask and vacuum-dried at 120 °C for 1 hour under an $N_2$ atmosphere. The temperature was then raised to 170 °C, and the Cs-OA stock solution (0.5 mL) was rapidly injected under vigorous stirring stirring 5-10 seconds. The reaction was quenched by immersing the flask into an ice-water bath. The precipitate was isolated via centrifugation (12000 rpm/min.), washed with hexane, and dispersed in toluene for reuse.

**Synthesis of ultrathin BiOBr**

Ultrathin BiOBr was synthesized using a previously reported solvothermal method. 1 mmol of KBr was added to 15 mL of ethanol and sonicated in an ultrasonic cleaner for 15 minutes. 1 mmol $Bi(NO_3)_3 \cdot 5H_2O$ was dissolved in 10 mL water under stirring conditions for 10 minutes. Next, add to the above solution and continue stirring for 20 minutes. The mixture was then transferred to a 50 mL Teflon-lined stainless-steel autoclave and heated at 150 °C for 4 hours. The resulting precipitates were washed with ethanol and deionized water, then dried at 60 °C overnight.

**Construction of heterojunction (Z-20)**

In a typical process, 10 mL of $CsPbBr_3$ colloidal solution (Toluene: 1 mg/mL) was mixed with an appropriate amount of BiOBr. The mixture was ultrasonicated for 15 minutes and stirred in the dark for 2 hours. It was then centrifuged at 12000 rpm for 5 minutes, washed with hexane, and vacuum dried at 60 °C for 12 hours. The different wt.% of $CsPbBr_3$ in the $CsPbBr_3$/BiOBr heterojunction is mentioned in Table S1.

CdS,[1] $WO_3$,[2] and $TiO_2$[3] were synthesized following previously reported methods. Further, the heterojunctions ($CsPbBr_3/WO_3$, CdS/BiOBr, and $TiO_2$/BiOBr) were constructed as shown in table S1.

**Table S1**. Description of the photocatalysts.

| S.N. | Photocatalyst-I | Photocatalyst-II | Heterojunction photocatalyst |
|---|---|---|---|
| 1 | 10 mg $CsPbBr_3$ | 90 mg BiOBr | Z-10 |
| 2 | 20 mg $CsPbBr_3$ | 80 mg BiOBr | Z-20 |
| 3 | 30 mg $CsPbBr_3$ | 70 mg BiOBr | Z-30 |
| 4 | 20 mg $CsPbBr_3$ | 80 mg $WO_3$ | $CsPbBr_3/WO_3$ |
| 5 | 20 mg CdS | 80 mg BiOBr | CdS/BiOBr |
| 6 | 20 mg $TiO_2$ | 80 mg BiOBr | $TiO_2$/BiOBr |

**Photoelectrochemical Experiments**

Photoelectrochemical measurements, including photocurrent response, electrochemical impedance spectra (EIS), and Mott-Schottky analyses, were conducted using a Metrohm Auto Lab M204 workstation under 100 W visible light illumination. The three-electrode setup consisted of a platinum wire as the counter electrode, an Ag/AgCl reference electrode, and a working electrode of FTO loaded with the 3 mg catalysts. The electrolyte used was 0.1 M tetrabutylammonium hexafluorophosphate ($TBAPF_6$) in ethyl acetate.

**Working electrode preparation and measurements**

The fluorine-doped titanium oxide (FTO) glass was initially cleaned by ultrasonication in ethanol and acetone, followed by rinsing with deionized water and isopropyl alcohol (IPA). Subsequently, 3 mg of catalyst was dispersed in 1 mL of toluene, 50 µL of 0.5 wt.% Nafion solution and sonicated for 10 minutes. A 500 µL suspension was then dropped onto a 1 $cm^2$ area of FTO and allowed to dry (room temperature) for about 50 minutes under ambient conditions. The photocurrent test was conducted against an Ag/AgCl reference electrode under blue LED visible light. Nyquist plots were recorded over a frequency range from 0.01 to $10^6$ Hz with an amplitude of 5 mV. Mott–Schottky measurements were conducted to determine the flat band potential of catalysts. This involves a direct current potential polarization technique with 500, 1000, and 1500 Hz fixed frequencies

**Figures and tables**

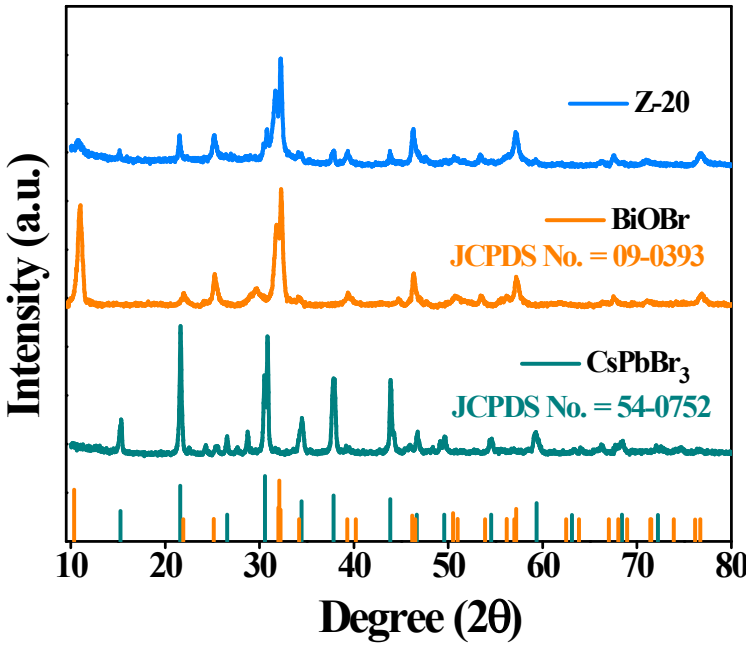


**Figure S1**. The PXRD patterns of $CsPbBr_3$, BiOBr, and Z-20.

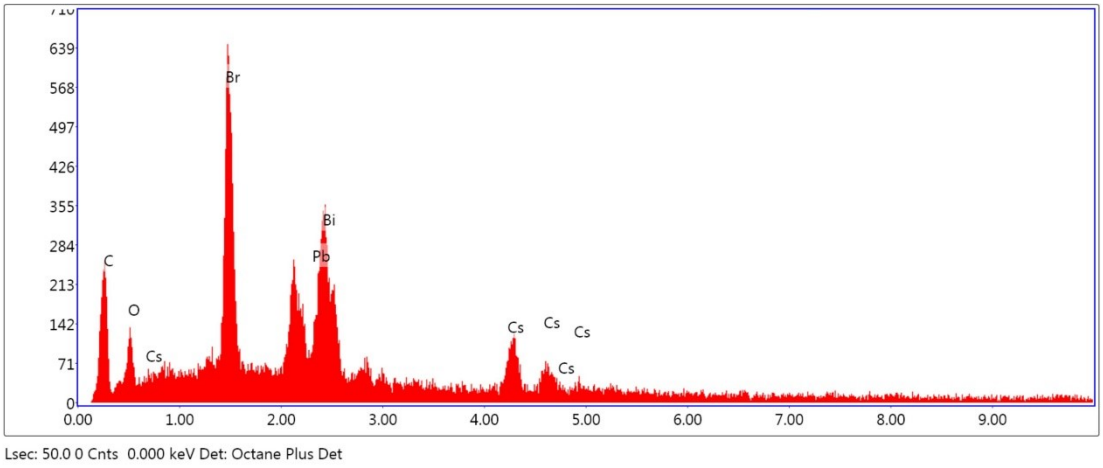


**Figure S2**. EDX spectrum of Z-20 showing Cs, Pb, Bi, O, and Br.

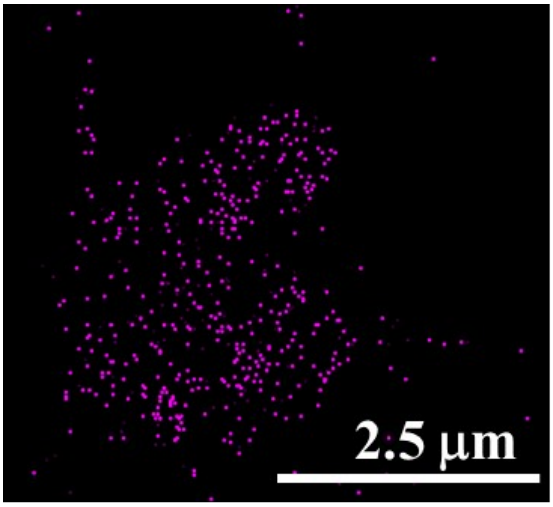


**Figure S3**. Elemental mapping of Z-20 showing O.

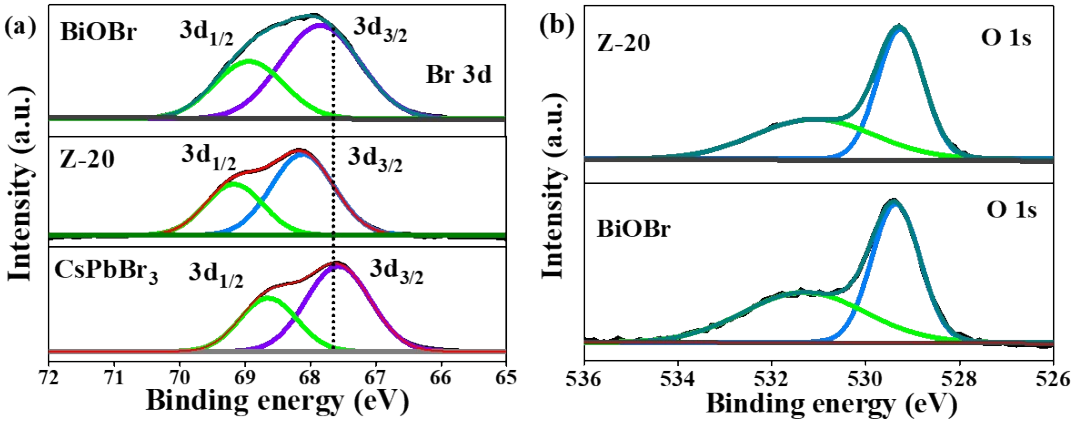


**Figure S4**. (a) Br 3d XPS of Z-20, $CsPbBr_3$, and BiOBr. (b) O 1s XPS of Z-20 and BiOBr.

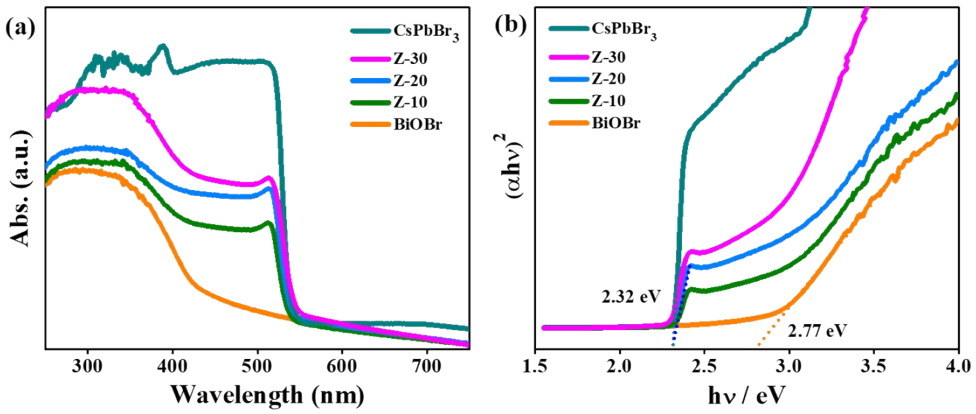


**Figure S5**. (a) UV-visible diffuse reflectance spectra (UV-DRS) of $CsPbBr_3$ QDs and BiOBr exhibit absorption maxima at 518 and 440 nm, whereas different wt.% of $CsPbBr_3$ QDs loaded on BiOBr NSs (Z-10, Z-20, and Z-30) exhibit absorption maxima at 518 nm. (b) Tauc plots of $CsPbBr_3$, BiOBr, and different wt.% of $CsPbBr_3$/BiOBr.

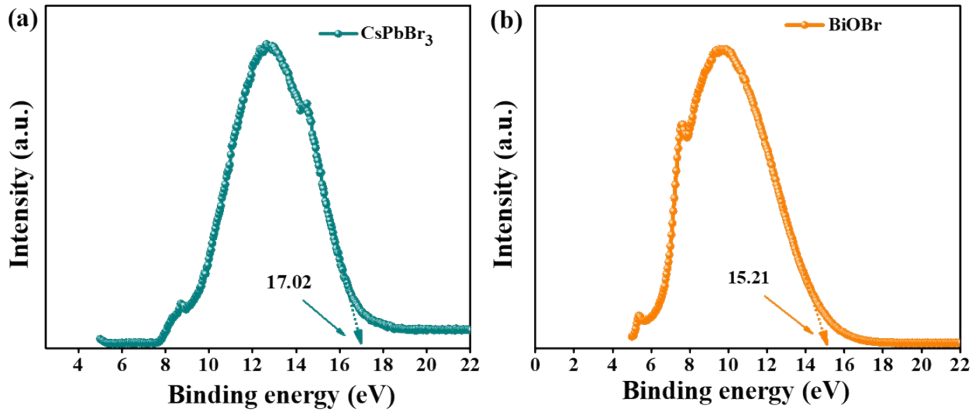


**Figure S6**. UPS spectra showing the secondary electron cut-off for $CsPbBr_3$ and BiOBr. The end energy levels (EEL) of $CsPbBr_3$ and BiOBr were measured to be 17.02 eV and 15.21 eV, respectively. Using the equation work function ($\Phi$) = 21.2 – EEL, $\Phi$ of $CsPbBr_3$ and BiOBr were calculated to be 4.2 eV and 6.01 eV, respectively.[4]

Based on the positions of the conduction bands, valence bands, and work functions of $CsPbBr_3$ and BiOBr photocatalysts, a direct Z-scheme charge transfer process is proposed for the $CsPbBr_3$/BiOBr Z-scheme heterostructure. When $CsPbBr_3$ and BiOBr, with their differing Fermi levels, form a heterojunction, an internal electric field is generated at the interface, directed from $CsPbBr_3$ to BiOBr.

Under the influence of this internal electric field, electrons and holes undergo reverse transfer, generating an electron flow that prolongs the lifetime of charge carriers and enhances the photocurrent response.

During the electron migration through the $CsPbBr_3$/BiOBr interface, the region near the BiOBr becomes negatively charged due to the accumulation of electrons. This leads to the formation of an electron accumulation layer and a downward bending of the BiOBr band edges. Conversely, the region near the $CsPbBr_3$ becomes positively charged, resulting in the formation of an electron depletion layer and an upward bending of the $CsPbBr_3$ band edges.

Driven by the internal electric field and the bending of interfacial bands, photogenerated electrons in the CB of BiOBr are transferred across the interface to recombine with holes in the VB of $CsPbBr_3$. This Z-scheme charge transfer mechanism enhances charge separation efficiency and improves the overall photocatalytic performance of the $CsPbBr_3$/BiOBr heterostructure.

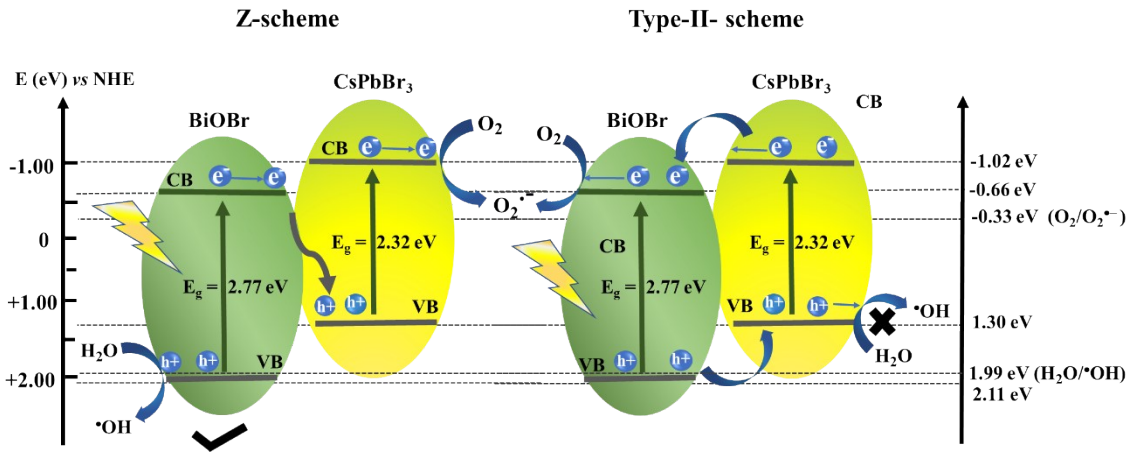


**Figure S7:** Schematic representation of Z-scheme and type-II heterojunctions. In the case of the Z-scheme mechanism, the valence band potential is high enough (2.11 $eV_{NHE}$ > 1.99 $eV_{NHE}$) to produce •OH radicals from $H_2O$. In contrast, for the Type-II heterojunction, the valence band potential is insufficient (1.30 $eV_{NHE}$ < 1.99 eV vs. NHE) to generate •OH radicals. In the type-II mechanism, electrons transfer from the CB of $CsPbBr_3$ to the CB of BiOBr, while holes migrate from the VB of BiOBr to the VB of $CsPbBr_3$, leading to the lowering of VBM. As a result, the valence band holes are no longer able to oxidize $H_2O$ to produce •OH radicals.

**Note:** Our experimental results support a Z-scheme pathway rather than a type-II mechanism. Importantly, no substantial difference in electronic band structure was found between the Z-scheme and S-scheme systems, since both are governed by similar interfacial charge transfer

dynamics: recombination of low-energy charge carriers (electrons in the CB of the less negative semiconductor and holes in the VB of the less positive semiconductor), while retaining the strong redox potentials of the remaining carriers.[5-9]

This model has been extensively employed in perovskite-based composites, including $CsPbBr_3$ systems, due to their favorable band alignment and recombination dynamics. Therefore, in this work, we adopt the Z-scheme description to explain the charge migration and redox pathways, as it aligns best with both our experimental observations and the enhanced photocatalytic behavior.[10-11]

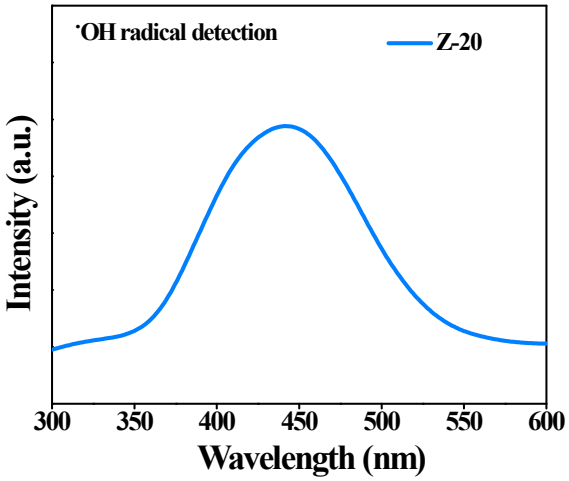


**Figure S8:** The •OH radicals were detected through photoluminescence analysis using the terephthalic acid-•OH adduct as a probe, showing a peak at 440 nm in the presence of Z-20.
**Reaction conditions**: For the detection of •OH radicals, a 0.25 mmol solution of terephthalic acid and 10 mg Z-20 were dispersed in an acetonitrile/water mixture at a ratio of 200:1 (3 mL). The solution was sonicated to make a uniform dispersion. After 1 h, 1 mL of the suspension was analyzed using a fluorescence spectrophotometer. The concentration of •OH radicals was determined by measuring the fluorescence intensity at 440 nm, with an excitation wavelength of 315 nm.

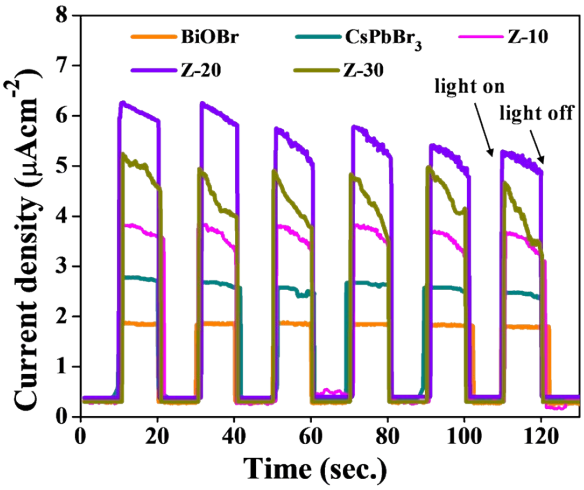


**Figure S9.** Photocurrent experiments confirmed the effective charge transfer and separation in the heterojunction photocatalysts. The photocatalyst Z-20 shows the highest photocurrent response compared to $CsPbBr_3$ and BiOBr and also Z-10, and Z-30.

We observed that the gradual attenuation of photocurrent under continuous illumination arises due to the effects of charge carrier trapping/recombination, surface state saturation, with band bending relaxation. These processes reduce free-carrier availability and weaken charge transfer kinetics, collectively diminishing photocurrent stability and intensity over time.[12-14]

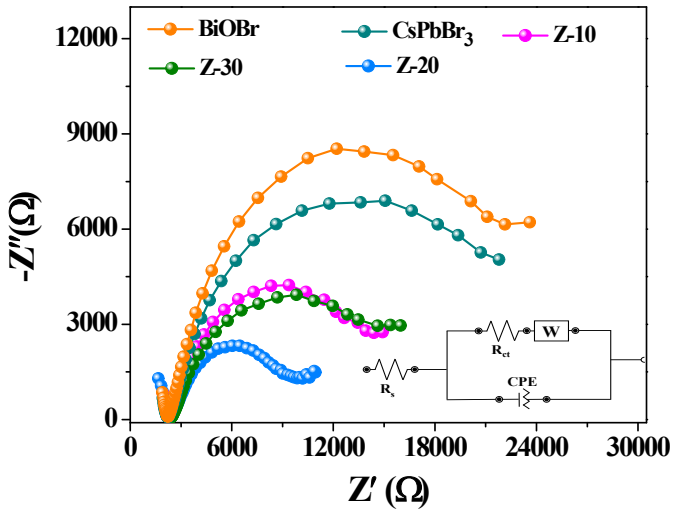


**Figure S10.** Electrochemical impedance spectra (EIS) of the photocatalysts under light irradiation. The Z-20 shows the lowest charge transfer resistance among the catalysts.

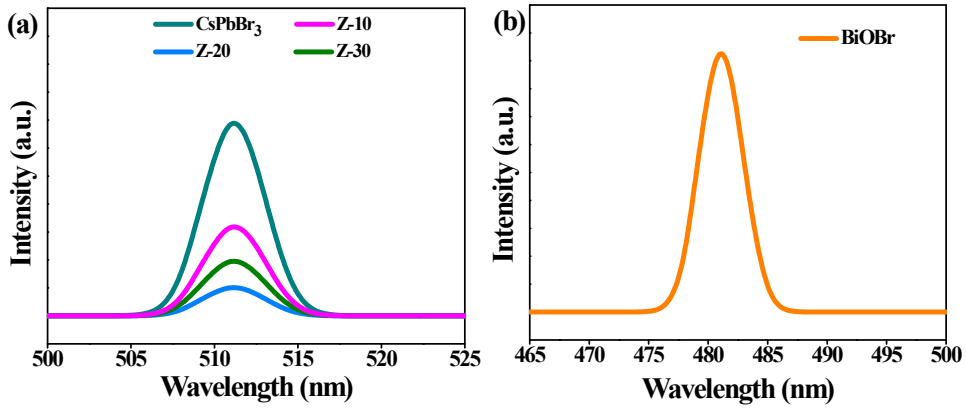


**Figure S11.** Photoluminescence (PL) spectra of the photocatalytic systems showed peaks at 510 nm for pristine $CsPbBr_3$ QDs and 483 nm for BiOBr. After the loading of $CsPbBr_3$ on BiOBr NSs, the PL intensity gradually decreases. The Z-20 photocatalyst exhibits the most effective charge carrier separation among all the catalysts.

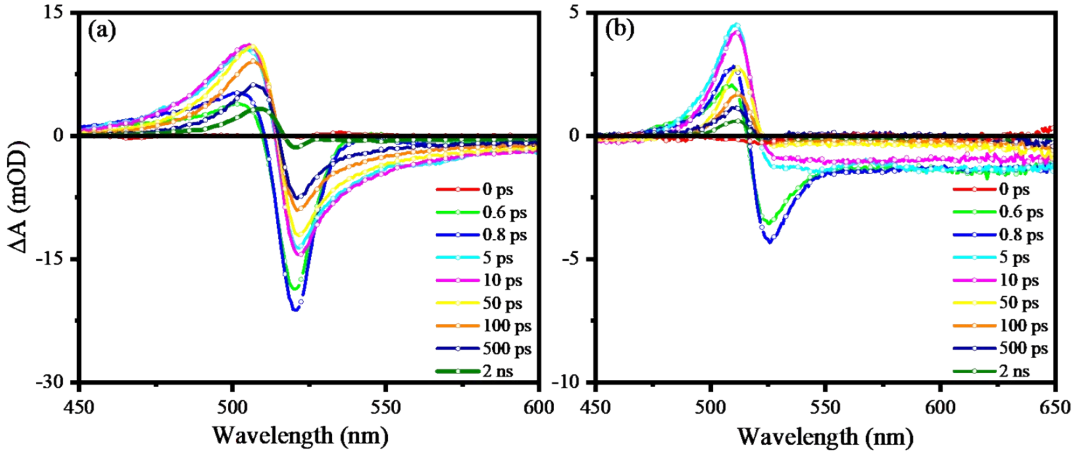


**Figure S12.** The transient absorption (TA) spectra at different delay times between pump and probe (a) $CsPbBr_3$, (b) Z-20.

**Table S2.** Fitting coefficient of kinetics traces at 490 nm, 500 nm, 550 nm, and 600 nm of $CsPbBr_3$ and Z-20 excited at 370 nm.

| Compound | Wavelength (nm) | $\tau_1$ (ps) ($a_1$) | $\tau_2$ (ps) ($a_2$) | $\tau_3$ (ps) ($a_3$) |
|---|---|---|---|---|
| $CsPbBr_3$ | 490 | 76 ± 10<br>0.0031 ±0.0004 | 800 ± 250<br>0.0022 ±0.0004 | Long Lived |
| | 500 | 100 ± 20<br>0.0040 ±0.0003 | 1300 ± 200<br>0.0044 ±0.0003 | Long Lived |
| | 550 | 60 ± 10<br>-0.0024 ±0.0005 | 750 ± 100<br>-0.0052 ±0.0005 | Long Lived |
| | 600 | 32 ± 3<br>-0.00056 ±0.00001 | 400 ± 70<br>0.0044 ±0.0003 | Long Lived |
| Z-20 | 490 | 3 ± 1<br>0.0013 ±0.0004 | 12 ± 4<br>-0.0007 ±0.0003 | Long Lived |
| | 500 | 20 ± 1<br>0.0019 ±0.0001 | 700 ± 100<br>0.0044 ±0.0003 | Long Lived |
| | 550 | 17 ± 0.2<br>-0.0014 ±0.0003 | 200 ± 22<br>-0.0023 ±0.0001 | Long Lived |
| | 600 | 0.4 ± 0.1<br>-0.0029 ±0.0003 | 13 ±2.2<br>-0.0013 ±0.0001 | Long Lived |

$$k_{trap} = \frac{1}{\tau_{Z-20}} - \frac{1}{\tau_{CsPbBr_3}} \qquad (1)$$

Where, $\tau_{Z-20}$ represents the lifetime of the bleach recovery of Z-20 and $\tau_{CsPbBr3}$ represents the lifetime of the bleach recovery of pristine $CsPbBr_3$ QDs.

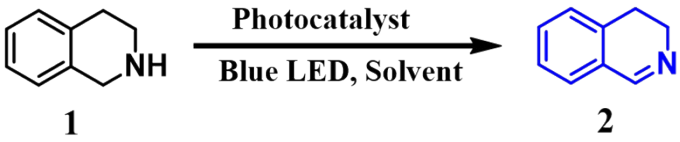


1 2

**Table S3**. Photocatalytic optimization condition of semi-dehydrogenation of 1,2,3,4-Tetrahydroisoquinoline.

| S.N. | Photocatalyst | Solvent | Conditions | Light/Dark | Time (h) | % Conversion of THIQ (1) | % Isolated Yield of DHIQ (2) |
|---|---|---|---|---|---|---|---|
| **Variation of catalysts** | | | | | | | |
| 1 | $CsPbBr_3$ | $CH_3CN$ | Air | Blue LED | 6 | Trace | Trace |
| 2 | BiOBr | $CH_3CN$ | Air | Blue LED | 6 | 57 | 56 |
| 3 | Z-10 | $CH_3CN$ | Air | Blue LED | 6 | 78 | 76 |
| **4** | **Z-20** | **$CH_3CN$** | **Air** | **Blue LED** | **6** | **99** | **97** |
| 5 | Z-30 | $CH_3CN$ | Air | Blue LED | 6 | 83 | 80 |
| **Variation of solvents** | | | | | | | |
| 6 | Z-20 | THF | Air | Blue LED | 6 | 69 | 64 |
| 7 | Z-20 | MeOH | Air | Blue LED | 6 | 85 | 77 |
| 8 | Z-20 | EtOH | Air | Blue LED | 6 | 89 | 81 |
| **9** | **Z-20** | **$CH_3CN$** | **Air** | **Blue LED** | **6** | **99** | **97** |
| 10 | Z-20 | 1,4-Dioxane | Air | Blue LED | 6 | 75 | 74 |
| 11 | Z-20 | Toluene | Air | Blue LED | 6 | 58 | 53 |
| 12 | Z-20 | DMF | Air | Blue LED | 6 | 33 | 28 |
| **Other variations in the reaction conditions** | | | | | | | |
| 13 | - | $CH_3CN$ | Air | Blue LED | 6 | No reaction | No reaction |
| 14 | Z-20 | $CH_3CN$ | Air | Dark | 6 | ~ 4 | ~ 4 |
| 15 | Z-20 | $CH_3CN$ | Pure $O_2$ | Blue LED | 3 | 99 | 97 |

**Reaction conditions:** 10 mg catalyst, 0.5 mmol 1,2,3,4-tetrahydroisoquinoline, and 3 mL solvent were mixed and irradiated with a 15 W blue LED light, maintaining a temperature of 34 ± 4 °C for the mentioned time period. *Isolated yields.

(a)

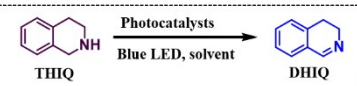


| S.N | Catalysts | Condition | Times (h) | THIQ Conv. (%) | DHIQ Yield (%) |
|---|---|---|---|---|---|
| 1 | $CsPbBr_3$ | Air | 6 | Trace | Trace |
| 2 | BiOBr | Air | 6 | 57 | 56 |
| 3 | Z-10 | Air | 6 | 78 | 76 |
| 4 | Z-20 | Air | 6 | 99 | 97 |
| 5 | Z-30 | Air | 6 | 83 | 80 |

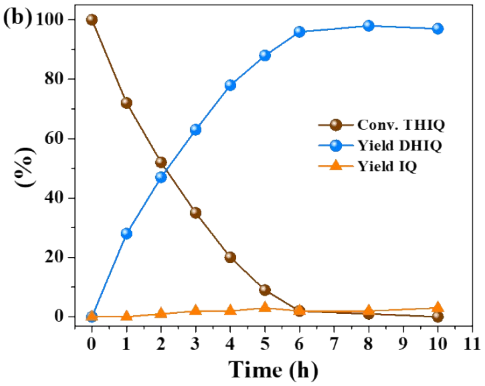


**Figure S13**. (a) Photocatalytic test with all catalysts. (b) Time-dependent conversion of 1,2,3,4-tetrahydroisoquinoline and DHIQ products formation with Z-20 heterojunction in the presence of air and light. After achieving the highest yield of DHIQ not convert into IQ with increasing reaction time.

**Reaction conditions:** 10 mg catalyst, 0.5 mmol THIQ, and 3 mL solvent were taken in a borosilicate reaction vial and irradiated with a 15 W blue LED at temperature of 34 ± 4°C for 10 hours. The catalyst was separated from the reaction mixture by centrifugation at 12,000 rpm for 10 minutes and used in the next cycle. The product was isolated by column chromatography on a silica column using varying ratios of ethyl acetate and hexane as the eluent. The product's isolated yield was reported in all cases.

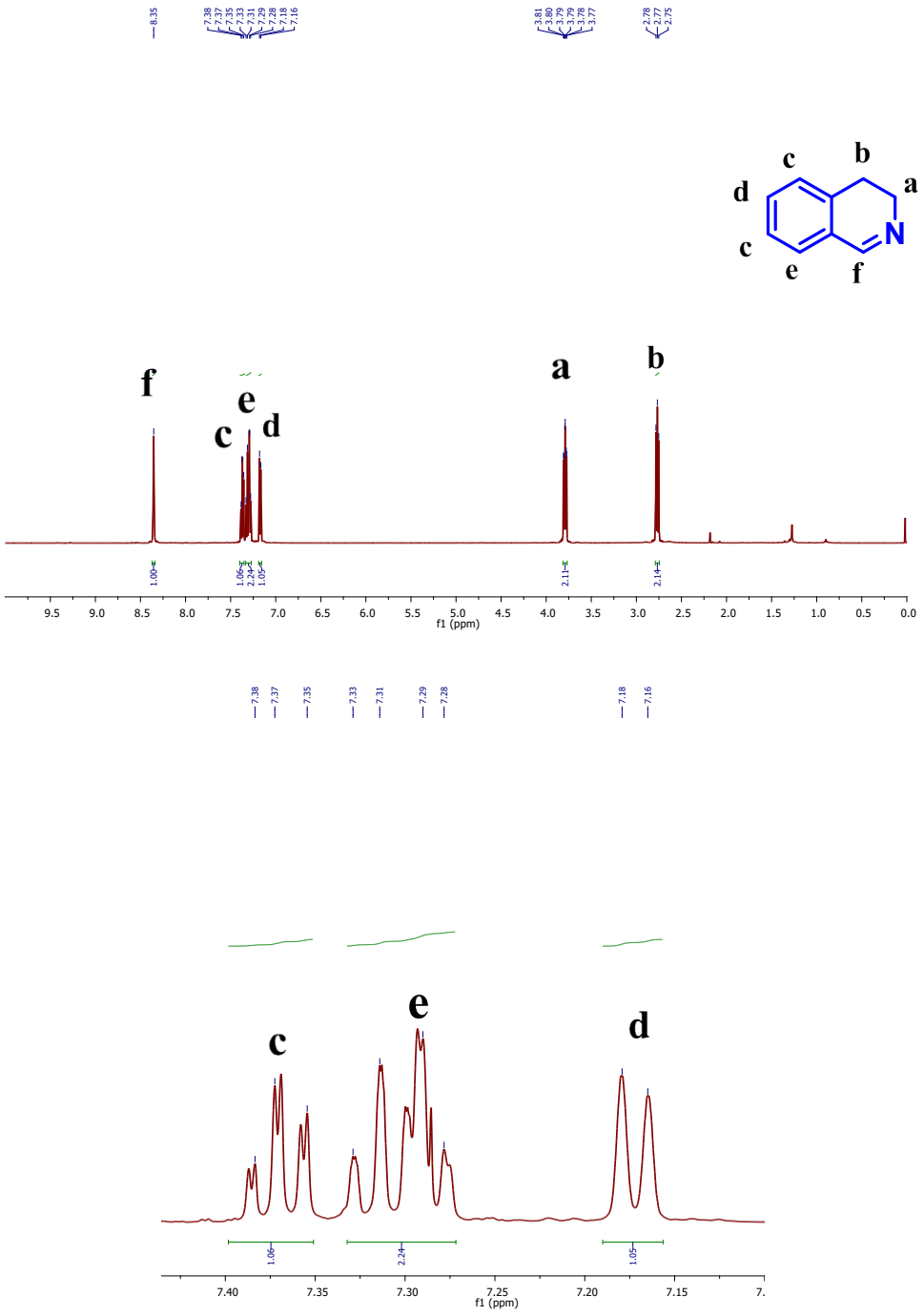


**Figure S14a:** $^{1}$H NMR spectrum of DHIQ, produced by the photocatalytic semidehydrogenation of THIQ with Z-20.

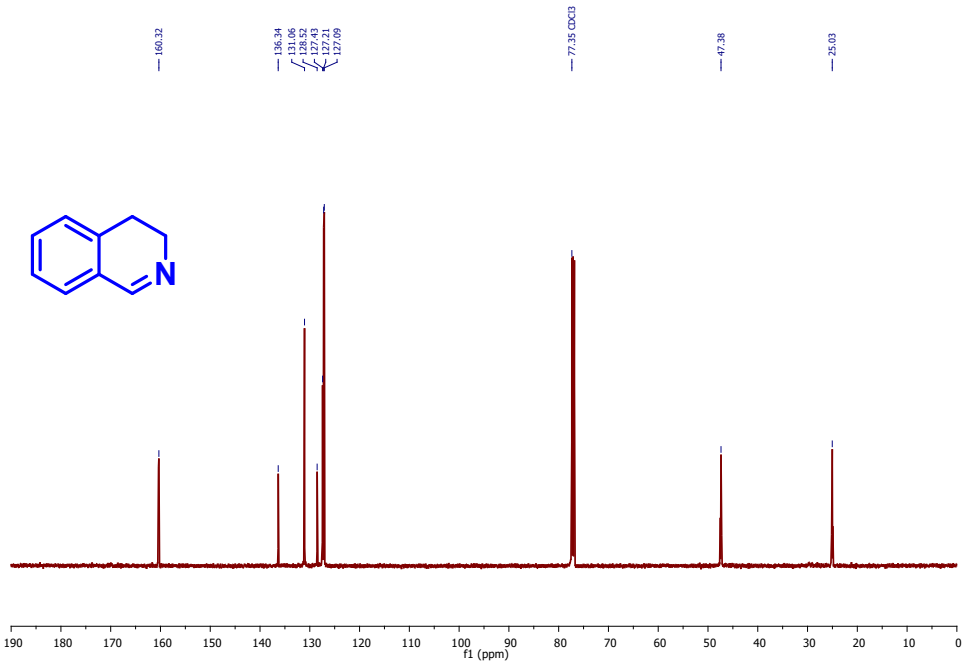


**Figure S14b:** $^{13}C$ NMR spectra of DHIQ, produced by the photocatalytic semidehydrogenation of THIQ with Z-20

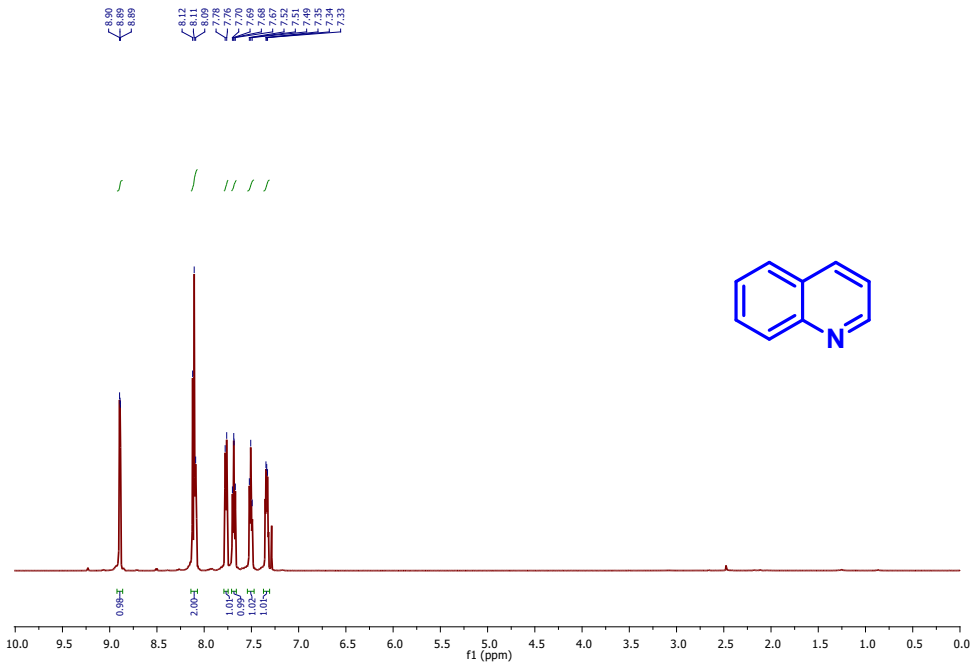


**Figure S15a:** $^{1}H$ NMR spectra of the separated product (IQ).

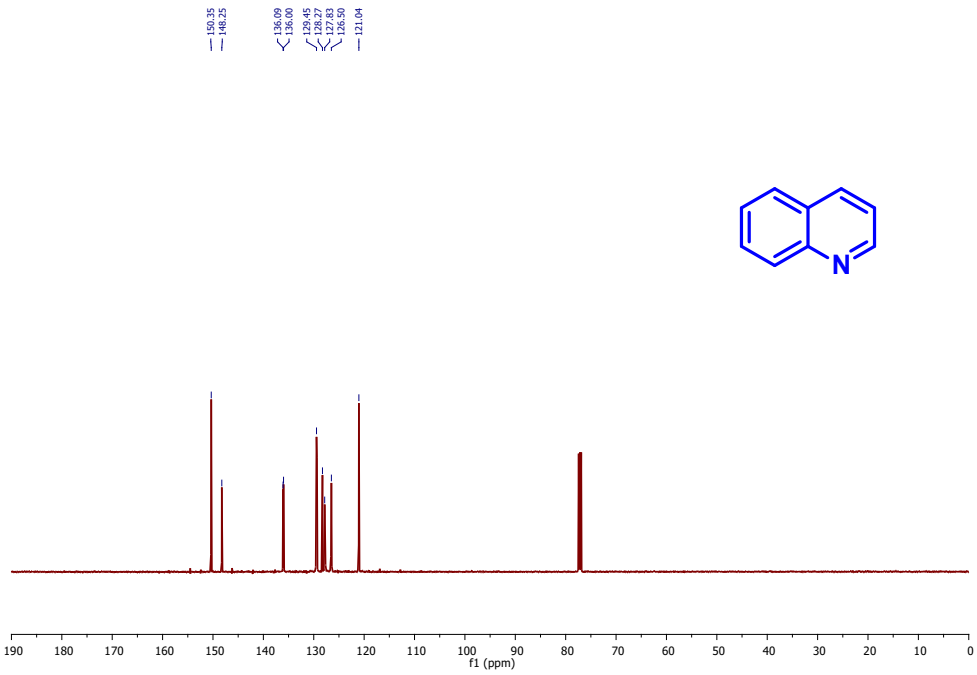


**Figure S15b:** $^{13}C$ NMR spectra of the separated product (IQ).

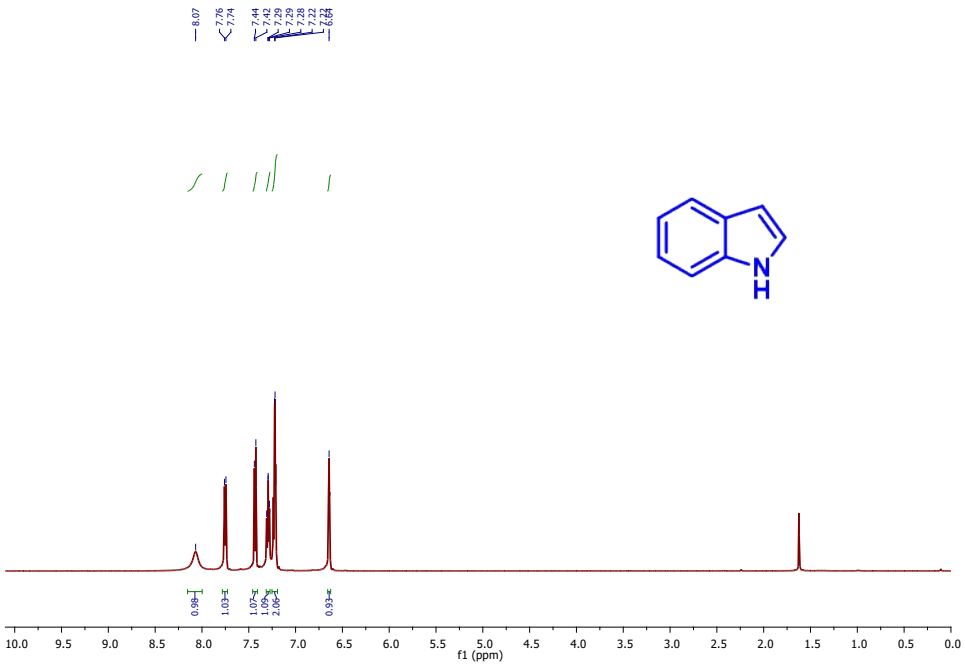


**Figure S16a:** $^{1}H$ NMR spectra of the separated indole product.

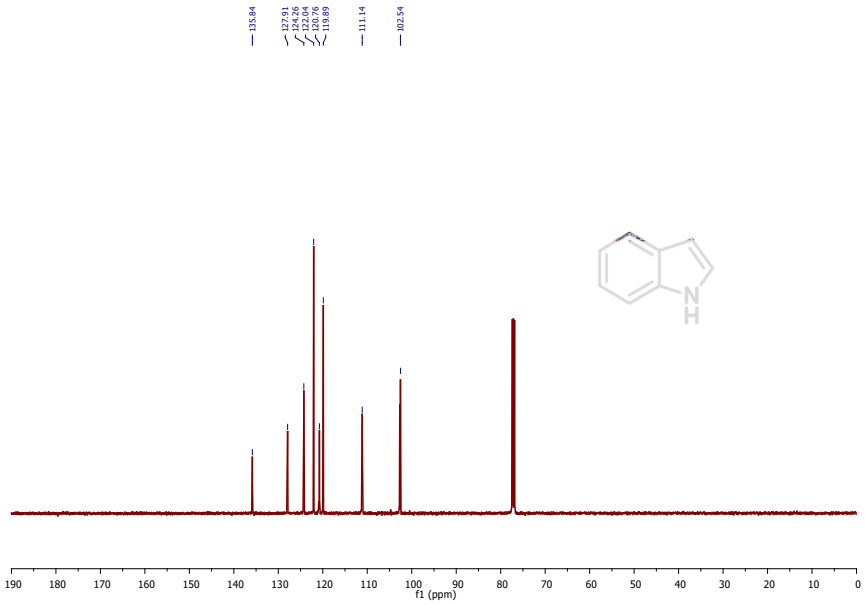


**Figure S16b:** $^{13}C$ NMR spectra of the separated indole product.

**Table S4**. Comparison of photocatalytic (semi)dehydrogenation of 1,2,3,4-tetrahydroisoquinoline using different photocatalyst systems.

| S.N. | Photocatalysts | Reaction conditions | DHIQ (% yield) and [formation rate (mmol $g_{cat}^{-1}$ $h^{-1}$)] | IQ (% yield) and [formation rate (mmol $g_{cat}^{-1}$ $h^{-1}$)] | Ref. |
|---|---|---|---|---|---|
| **IQ selective (4 electron transfer)** | | | | | |
| 1 | *h*-BCN | Blue LEDs, 12 h | - | 87 [2.17] | [15] |
| 2 | $Ni(OH)_2$@CdSe/CdS | 420 nm LED, 24 h | - | 38 [0.02] | [16] |
| **Mixture of IQ and DHIQ** | | | | | |
| 3 | Ni-$TiO_2$ | Visible light, TEMPO, 24 h | 52 [0.86] | 42 [0.70] | [17] |
| 4 | Rh/$TiO_2$ | Blue LED 453 nm, Ar, 48 h | 48 [0.40] | 39 [0.32] | [18] |
| **DHIQ selective (2 electron transfer)** | | | | | |
| 5 | $MoS_2/ZnIn_2S_4$ | 300W Xe arc lamp, $N_2$, 12 h | 99 [0.83] | - | [19] |
| 6 | $ZnIn_2S_4$ | 300 W Xe light, air, 7 h | 98 [1.40] | - | [20] |
| 7 | $Zn_3In_2S_6$ | 300 W visible light, 20 min | 99 [62.1] | - | [21] |
| 8 | MOF-CdS | Xe lamp, Ar, 12 h | 53 [0.29] | - | [22] |
| **9*** | **$CsPbBr_3$** | **15 W Blue LED, 6 h** | **ND** | **ND** | **This work** |
| **10*** | **BiOBr** | | **56** [4.60] | **5** | |
| **11*** | **BiOBr/$CsPbBr_3$ (Z-20)** | | **97** [8.08] | **Trace** | |

*Isolated yield

ND = not detected

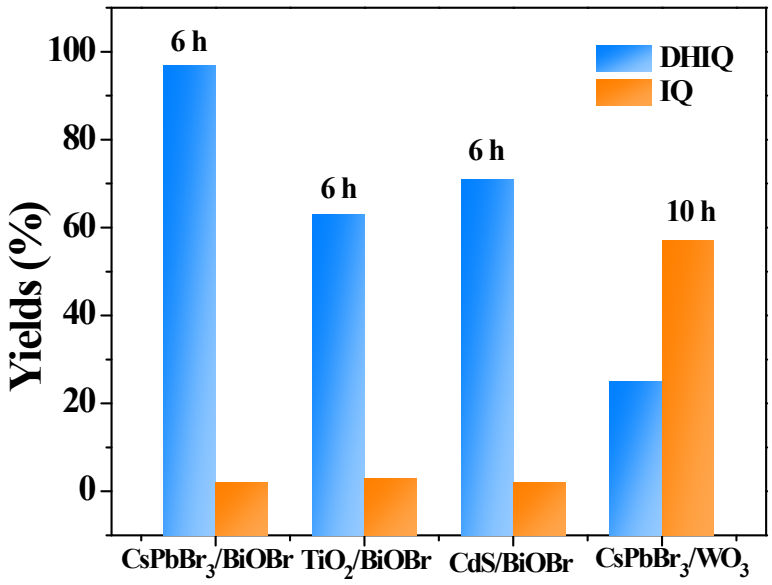


**Figure S17**. Different heterostructure photocatalysts for semidehydrogenation of THIQ in air.

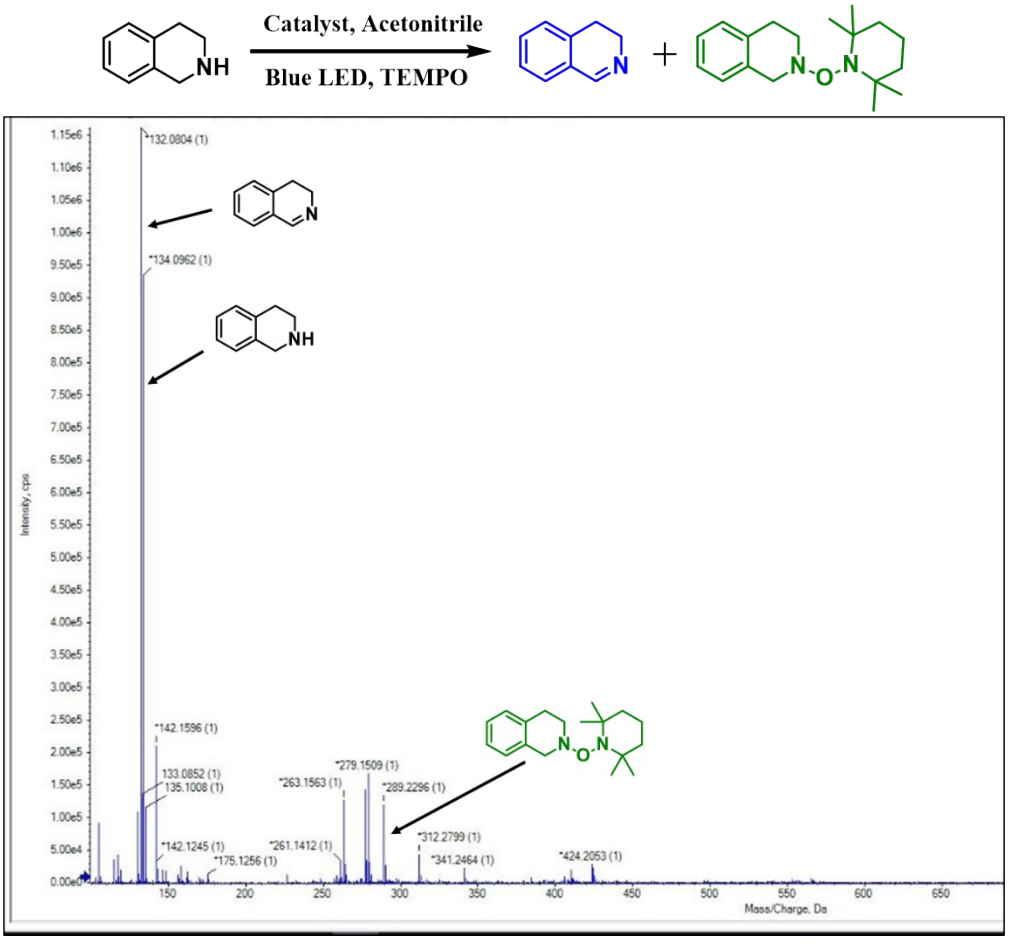


**Figure S18:** Mass spectrometry detected the THIQ-TEMPO (2,2,6,6-tetramethyl-1-piperidinyloxyl) adduct.

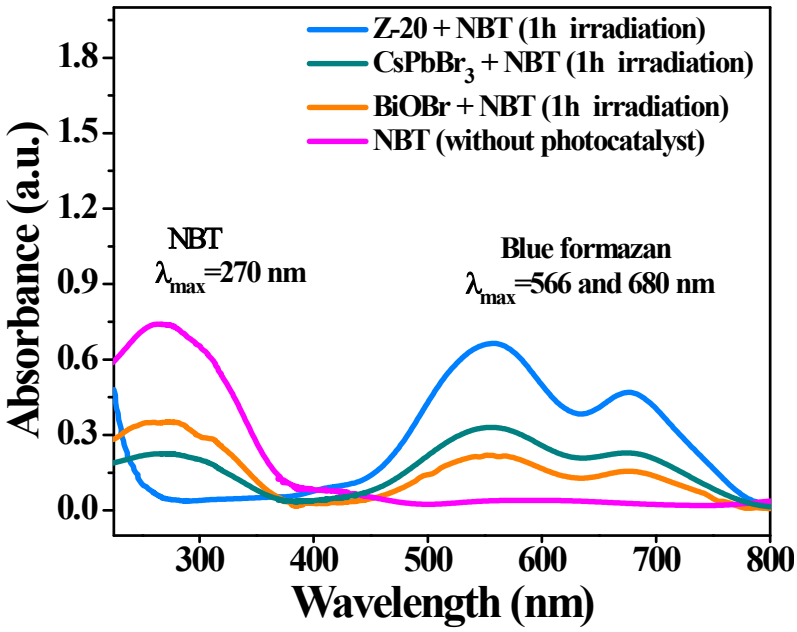


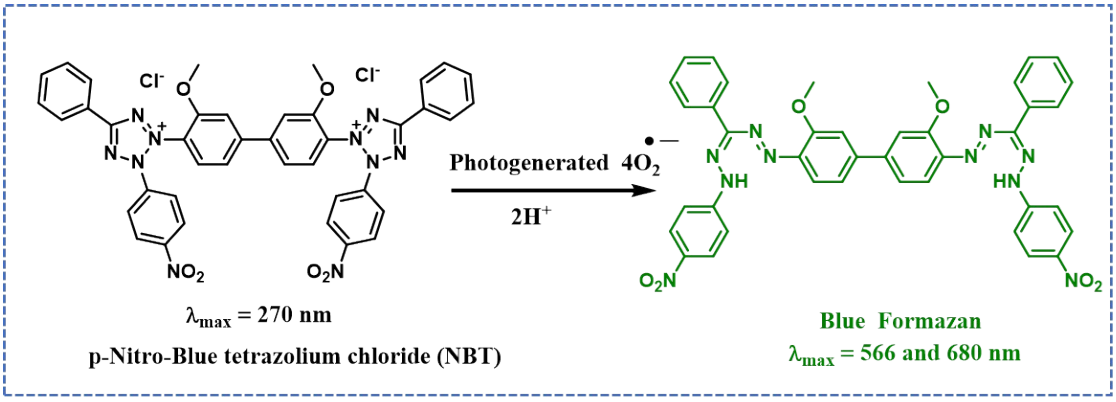


**Figure S19**. Detection of photogenerated superoxide radicals.

**Reaction conditions:** 10 mg photocatalyst was dispersed in 2 mL of acetonitrile, and then 150 μL of NBT (150 μmol/L) aqueous solution was added. After thorough mixing, the solution was illuminated with a 15 W blue LED for 1 hour, then centrifuged at 12,000 rpm for 5 minutes. The supernatant was analyzed using UV–vis spectroscopy. *P*-nitro-blue tetrazolium chloride (NBT) was used as an indicator for superoxide anion radicals, which reduce NBT to form blue formazan in the presence of $O_2^{\bullet-}$. The UV characteristic absorption peaks of formazan are around 566 nm and 680 nm.

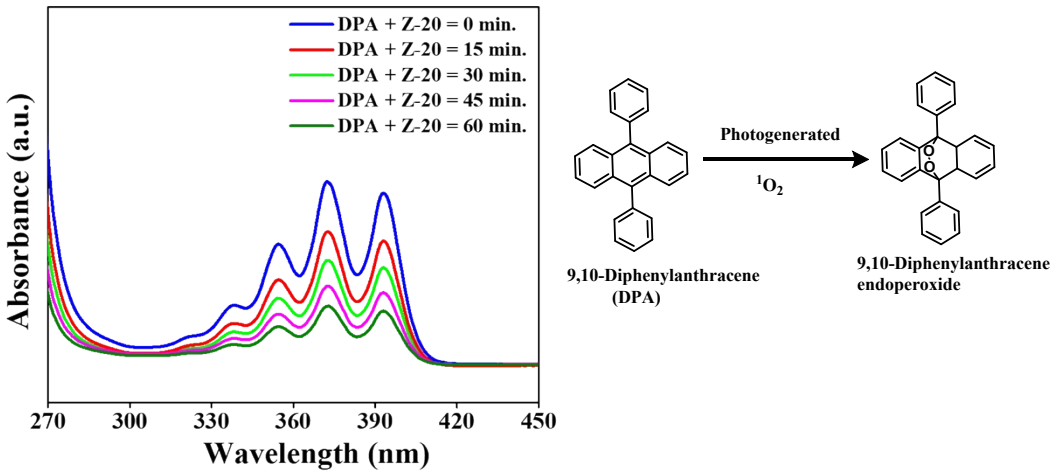


**Figure S20**. UV-visible spectroscopy detects the photogenerated $^1O_2$.[23]

The production of $^1O_2$ in solution was detected using 9,10-diphenylanthracene (DPA) as a $^1O_2$ probe.

**Reaction condition:** 10 mg (Z-20) was mixed with DPA (0.05 mmol) solution in acetonitrile-DMSO (99:1 v/v) and irradiated with light. The aliquot was collected at different time intervals. The catalyst was separated from the reaction mixture by centrifugation, and the absorbance of the solution was recorded.

**Note:** DMSO (1%, v/v) was added only to improve DPA solubility, and such minimal levels in acetonitrile do not affect selective $^1O_2$ trapping or quantification, especially in predominantly acetonitrile solutions.

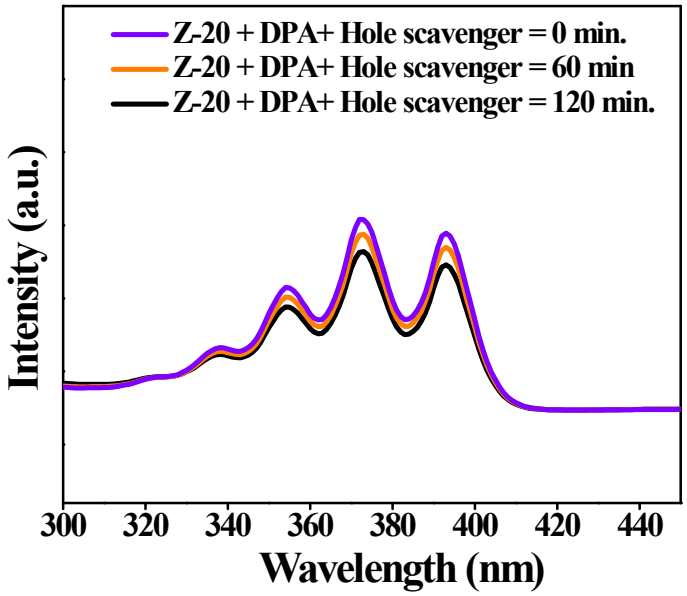


**Figure S21**. $^1O_2$ generation through the reaction ($O_2^{\bullet-} + h^+ \rightarrow {}^1O_2$) process, detected by UV-visible spectroscopy in the presence of a hole scavenger in a reaction mixture of Z-20 and DPA solution. The hole scavenger prevented the interaction of $O_2^{\bullet-}$ with holes and reduced the generation of $^1O_2$, resulting in a negligible change in the peak intensity.[24-26]

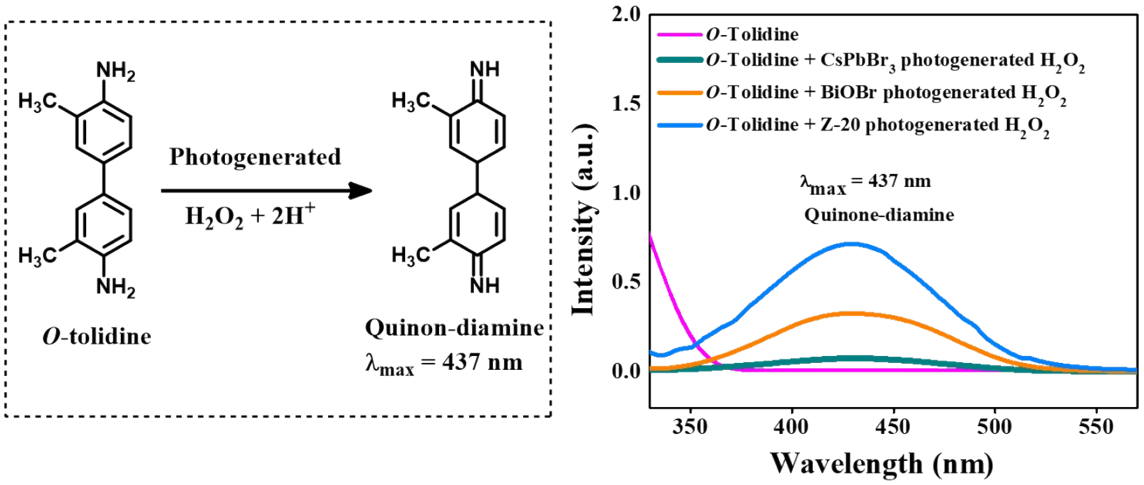


**Figure S22**. UV-visible spectroscopy detects the photogenerated $H_2O_2$ in the reaction mixture. The oxidation of *o*-tolidine by $H_2O_2$ produces blue-colored quinone-diamine, which has a maximum absorbance of 437 nm.

**Reaction conditions:** 0.5 mmol THIQ, 10 mg Z-20, and 2 mL acetonitrile at 6 h irradiation, and the Z-20 was separated by centrifugation at 12,000 rpm for 10 minutes. The separated reaction solution was workup with 2 mL water and 5 mL ethyl acetate using a separating funnel, the whole reaction mixture was divided into two layers, and the photogenerated $H_2O_2$ was separated in water from the reaction mixture. A 10 µL aliquot mixture of (water and photogenerated $H_2O_2$) was added to 1 mL *O-tolidine* solution (1 wt.% *O-tolidine* in 0.1 M HCl), and UV-visible spectra were recorded.

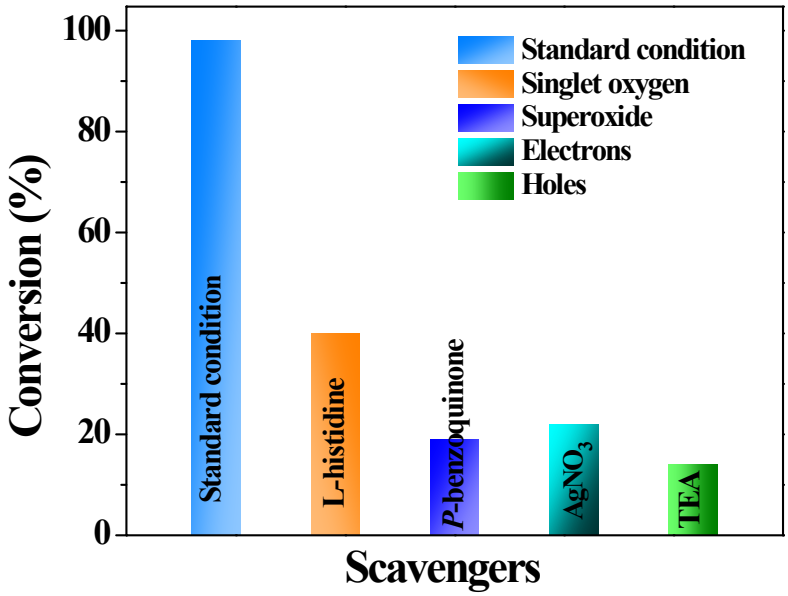


**Figure S23.** Quenching experiments confirmed the formation of holes, electrons, and radicals in the reaction mixture. *L*-histidine, *para*-benzoquinone, $AgNO_3$, and triethylamine (TEA) were used as scavengers for superoxide radicals, free radicals, electrons, and holes, respectively.

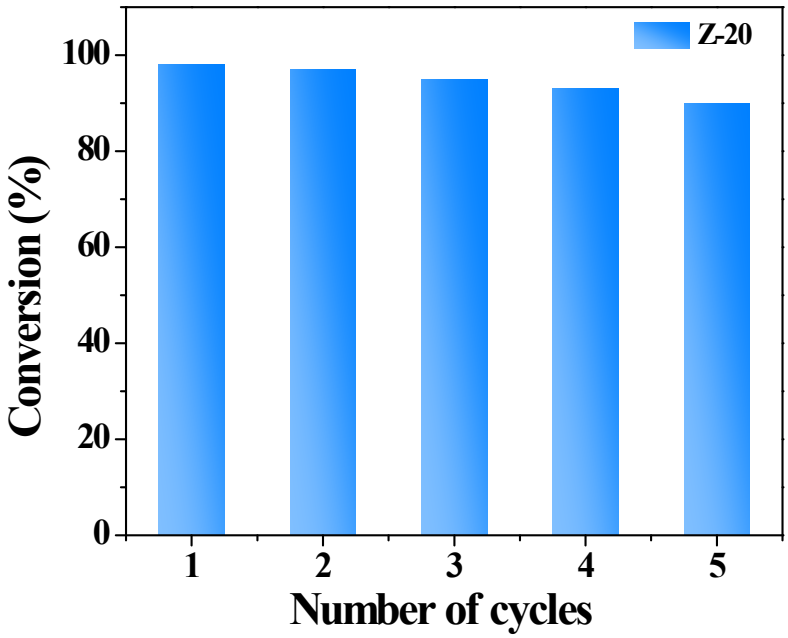


**Figure S24**. Recyclability of Z-20 photocatalyst for semidehydrogenation of THIQ in air.

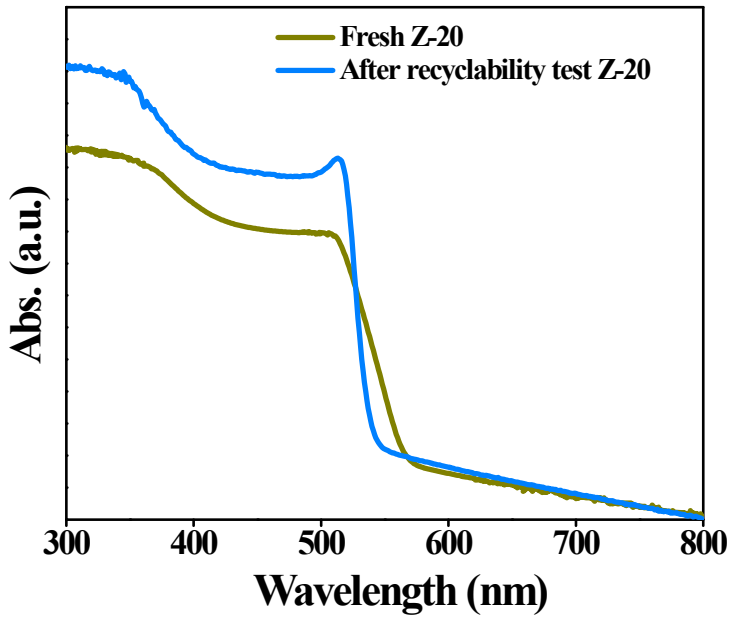


**Figure S25**. UV-vis-DRS of Z-20 after five cycles in air.

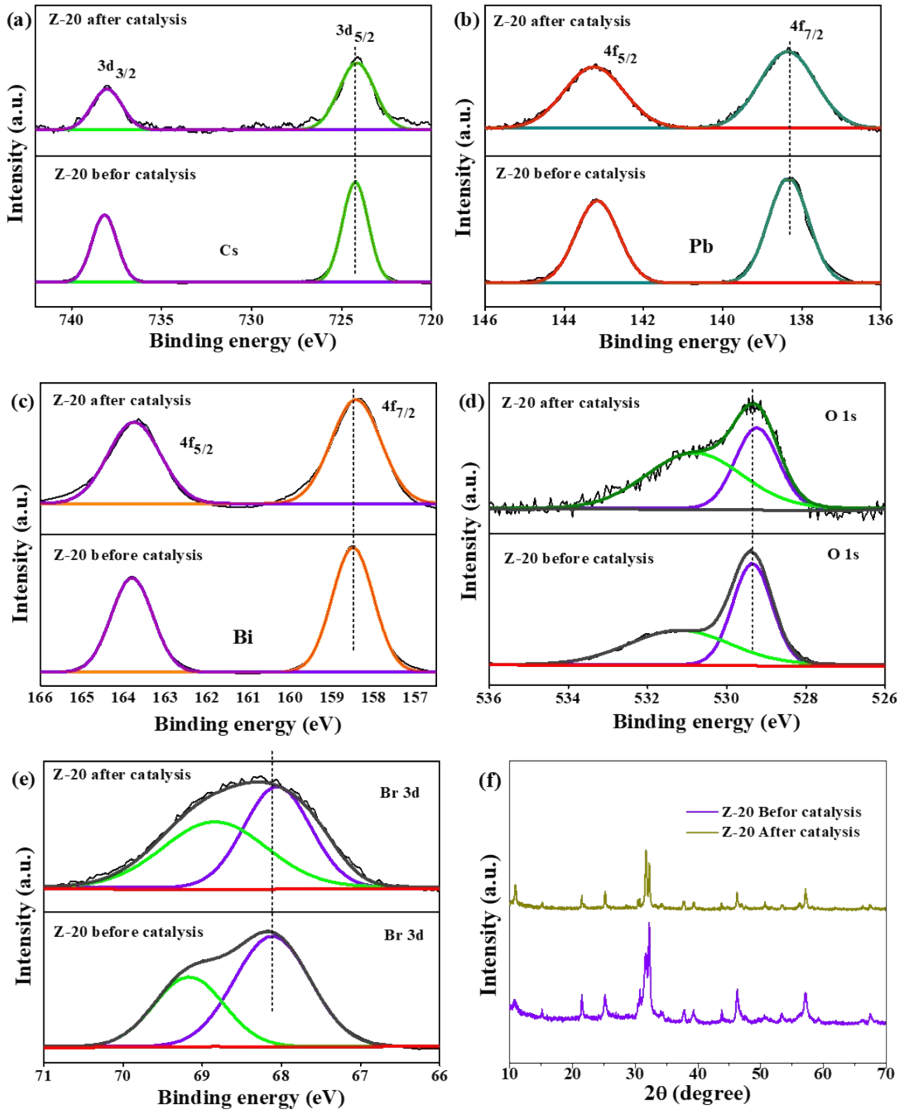


**Figure S26**. After the catalysis, XPS (a-e) and (f) PXRD study.

## References


1 A. K. Singh, A. Jaryal, S. K. Patel, D. Kumar, E. S. Subramaniam Iyer, K. Kailasam and A. Indra, *J. Mater. Chem. A* 2023, **11**, 16724–16733.

2 A. Singha, J. Kaishyop, T. S. Khan, and B. Chowdhury, *ACS Appl. Nano Mater.* 2023, **6**, 21818–21828.

3 J. Qiu, P. Zhang, M. Ling, S. Li, P. Liu, H. Zhao, and S. Zhang, *ACS Appl. Mater. Interfaces* 2012, **4**, 3636–3642.

4 Z. H. Zhao, H. Wang, J. Li, X. Qiao, Z. Liu, Z. Ren, M. Yuan and J. Zhang, *J. Am. Chem. Soc.* 2024, **146**, 29441-29449.

5 Z. Zhang, L. Li, Y. Jiang, and J. Xu, *Inorg. Chem.*, 2022, **61**, 3351-3360.

6 W. Sun, J. Liu, F. Ran, N. Li, Z. Li, Y. Li, and K. Wang, *Dalton Trans.*, 2024, **53**, 14018.

7 L. Zhang, J. Zhang, J. Yu, and H. García, *Nat. Reviews Chem.*, 2025, **9**, 328–342
8 S. Ghasemi, A. Parastesh, M. Padervand, H. Ren, X. Li, A. Labidi, M. Signoretto, E.A. Dawi, Hamzehlouyan, E. Lichtfouse, and C. Wang, C*urrent Opinion in Chem. Eng.*, 2025, **47**, 101059.
9 G. Rana, P. Dhiman, A. Kumar, A. Chauhan, and G. Sharma, *Environ. Sci. and Pollution Research*, 2024, **31**, 40851-40872.
10 S. Mansingh, K.K. Das, N. Priyadarshini, D.P. Sahoo, D. Prusty, J. Sahu, U.A. Mohanty, and K. Parida, *Energy & Fuels*, 2023, **37**, 9873-9894.
11 I. Ullah, P. Zhao, N. Qin, S. Chen, J.H. Li, and A.W. Xu, *The Chem. Record*, 2024, **24**, 202400127.
12 L.M. Peter, A.B. Walker, T. Bein, A.G. Hufnagel, and I. Kondofersky, *J. Electro. Chemi*, 2020, **872**, 114234.
13 J. Y. Loh, G. Sharma, N.P. Kherani, and G.A. Ozin, *Adv. Energy Mater.*, 2021, **11**, 2101566.
14 W. Yang, R.R. Prabhakar, J. Tan, S.D. Tilley, and J. Moon, *Chem. Soc. Rev.*, 2019, **48**, 4979-5015.
15 M. Zheng, J. Shi, T. Yuan, and X. Wang, *Angew. Chem. Int. Ed.* 2018, **57**, 5487–5491.
16 Y. Liu, T. Yu, Y. Zeng, J. Chen, G. Yang and Y. Li, *Catal. Sci. Technol.* 2021, **11**, 3810–3817.
17 N. O. Balayeva, N. Zheng, R. Dillert, and D. W. Bahnemann, *ACS Catal.* 2019, **9**, 10694–10704.
18 N. O. Balayeva, Z. Mamiyev, R. Dillert, N. Zheng, and D. W. Bahnemann, *ACS Catal.* 2020, **10**, 5542–5553.
19 M. Hao, X. Deng, L. Xu and Z. Li, *Appl. Catal. B Environ.* 2019, **252**, 18–23.
20 X. Yin, B. Lv, Y. Kang, X. Xu, X. Lei, L. Li, H. Wang, H. Xi, J. Yang and Z. Yang, *Catal. Lett.* 2023, **153**, 570–583.
21 J. Luo, X. Wei, Y. Qiao, C. Wu, L. Li, L. Chen, and J. Shi, *Adv. Mat.* **2023,** 35, 2210110.
22 X. Y. Lin, M. Y. Qi, Z. R. Tang, Y. J. Xu, *Appl. Catal. B Environ.* **2022**, *317*, 121708.
23 N. Singh, R. SenGupta, S. Bose, *Nanoscale* **2024**, *16*, 3243–3268.
24 N. Singh, R. S. Gupta, S. Bose, *Nanoscale* 2024, **16**, 3243–3268.
25 Y.J. Zhang, J.J. Chen, and H. Q. Yu, *Chem. Eng. Journal*, 2022, **446**, 137237.
26 J.M. Aubry, B. Cazin, and F. Duprat, *J. Org. Chem.*, 1989, **54**, 726-728.